CHEMISTRY OF MATERIALS

ARTICLE

pubs.acs.org/cm

Behavior of Li Guest in KNb_5O_{13} Host with One-Dimensional Tunnels and Multiple Interstitial Sites

Yuhao Lu,[†,‡] John B. Goodenough,[*,†,‡] Gopi Krishna Phani Dathar,[†,§] Graeme Henkelman,[†,§] Jing Wu,[§] and Keith Stevenson[†,§]

[†]Energy Frontier Research Center (EFRC), [‡]Texas Materials Institute, and [§]Department of Chemistry and Biochemistry, University of Texas at Austin, Austin, Texas 78712, United States

ABSTRACT: Potassium niobium oxide (KNb_5O_{13}) exhibits multiple unoccupied interstitial sites in its crystal structure. In a lithiation/delithiation process, ~3.5 Li^+ ions can be inserted/extracted into/from these sites above 1.0 V vs Li/Li^+. Although there are two-dimensional tunnels in KNb_5O_{13}, the experiment demonstrates that only *a*-axis tunnels have access to the electrolyte for the lithiation/delithiation process. The one-dimensional tunnels connect to multiple off-axis sites (4*c*, 4*d*, and 8*e*), which results in a polarization hysteresis in the potential profile of the lithiation/delithiation process. Using experimental and calculation methods, the study explains the polarization hysteresis with a proposed lithiation/delithiation process in KNb_5O_{13}.

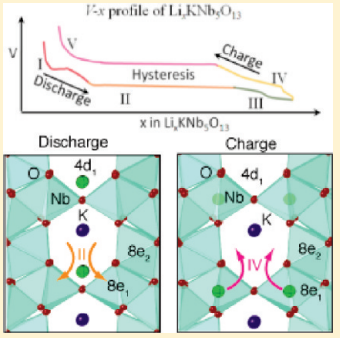

KEYWORDS: niobate anode, oxide Li host, lithiation/delithiation hysteresis

INTRODUCTION

The demonstration of reversible lithium insertion into oxide hosts[1−4] has made the advent of the Li^+-ion battery possible. However, the organic liquid-carbonate electrolytes used have an energy gap (E_g) between their lowest unoccupied molecular orbital (LUMO) and highest occupied molecular orbital (HOMO) located between 1.1 V and 4.3 V versus Li^+/Li^0, which makes the electrochemical potential (the Fermi energy) of lithium poorly matched to the electrolyte LUMO. In an investigation of the position of the Nb(V)/Nb(IV) redox energy in an oxide relative to the LUMO of the carbonate electrolyte,[5] a study of the reversible lithium insertion into KNb_5O_{13} of up to 3.5 Li/formula unit showed an unusual hysteresis of the voltage profile, which indicated that, unlike in a conventional Li-insertion host, the sequence of interstitial sites occupied by the Li^+ upon insertion is different from that upon extraction. In this study, only the magnitude of hysteresis was slightly increased upon increasing the current densities from 15 mA/g to 30 mA/g to 60 mA/g; but the voltage profile was not changed. Therefore, the Nernst equation coupled with slow diffusion is not the cause of the hysteresis shape observed; this shape would seem to represent a difference in the path sequence on Li insertion and extraction.[6] Since the voltages 1.0 V < *V* < 2.0 V versus Li^+/Li^0 are below the kinetic LUMO of the electrolyte, there is no formation of a passivating SEI layer to complicate the interpretation of this phenomenon. Therefore, we have undertaken modeling and a further experimental study to clarify the insertion versus extraction process.

The synthesis and structure of KNb_5O_{13} was first reported by Kwak et al.[7] The orthorhombic (*Pbcm*) structure with four formula units per unit cell is shown in Figure 1, projected along the *a*-axis. The Nb atoms occupy three distinguishable octahedral sites, 8*e*, and 4*c* symmetry sites. Two-dimensional *a*−*b* slabs contain edge-shared $Nb_2-Nb_3-Nb_2$ triples sharing edges with 180° $Nb_2-O_7-Nb_2$ bridges connecting the *a*−*b* slabs; the triples are bridged by corner-sharing Nb_1 octahedra. This peculiar configuration of NbO_6 octahedra leaves open *a*-axis and *b*-axis channels occupied by the large K^+ ion. Displacement of the K^+ ion in the *b*-direction from the axis of the *a*-axis tunnels leaves open $4d_1$ positions along the *a*-axis between K^+ ions; $4d_2$ positions between K^+ ions along the *b*-axis are also available within the *a*-axis tunnels, as shown in Figure 2. Within the slabs, empty $8e_1$, $8e_2$, and $4c_1$ sites are also available to Li^+.

EXPERIMENTAL SECTION

KNb_5O_{13} was synthesized from potassium carbonate (Alfa, 99.9%) and niobium pentoxide (Alfa, 99.9%) used directly without further purification. The starting materials were mixed for at least 30 min in an agate mortar, preheated at 400 °C for 5 h to remove carbon dioxide, and then pressed into a small pellet that was sintered in an alumina crucible at 800 °C for three days; the product was cooled to room temperature naturally. A low reaction temperature and a long time period were adopted to reduce the evaporation of K_2O and remove impure phases.

Powder X-ray diffraction (XRD) patterns were obtained with a Philips X-ray diffractometer using Cu Kα radiation (λ = 1.5418 Å). The work current in the X-ray tube was 35 mA; the voltage was 40 kV. The angular resolution in 2θ scans was 0.02° over a 2θ range of 10°−80°. The XRD results were refined with the Material Analysis Using Diffraction (MAUD) program and the Rietveld method.[8] Raman spectra were obtained with a Renishaw inVia Raman Microscope with a 514.5-nm green laser beam. X-ray photoelectron spectroscopy (XPS) data were acquired with a Kratos AXIS 165 Multitechnique Electron Spectrometer (Manchester, U.K.).

Received: April 4, 2011
Revised: May 19, 2011
Published: June 08, 2011

A standard CR2032 coin cell was adopted to evaluate the lithiation/delithiation process of KNb_5O_{13}. The coin cell included a sandwich structure of a KNb_5O_{13} cathode, a Celgard polypropylene separator, and a piece of lithium metal as the anode. The KNb_5O_{13} electrode consisted of 87 wt % KNb_5O_{13}, 5 wt % polytetrafluoroethylene (PTFE) binder, and 8 wt % acetylene black. The electrode was rolled into a thin sheet and punched into circular disks. The typical electrode mass was 6 ± 2 mg. The electrolyte used for testing was 1 M $LiPF_6$ in 1:1 EC/DEC (vol/vol). All cells were assembled in an argon-filled glovebox. The cells were aged for 5 h before charge/discharge to ensure full absorption of the electrolyte into the electrode. The electrodes for characterization by XRD, Raman, and XPS were obtained from cells that were charged or discharged to the targeted potential at a fixed current density of 20 mA/g and then kept at the potential until the current was $<10^{-9}$ A, or the step time lasts 1 day, in order to reach the stable states of Li^+-ion diffusion in KNb_5O_{13}.

COMPUTATIONAL METHODS

The electronic structure calculations were performed with density functional theory (DFT) as implemented in the Vienna ab initio simulation package (VASP)[9,10] with the PBE functional[11] and projector augmented-wave[12]-based pseudopotentials. The initial structure for KNb_5O_{13} was built from data in the ICSD database. A plane wave cutoff of 500 eV was used with a Monkhorst-Pack grid with k-point mesh spacing of 0.05 $Å^{-1}$ to sample the Brillouin zone. All calculations were spin-polarized. Geometry optimizations were considered converged when the force on each atom was <0.005 eV $Å^{-1}$. Binding energies of Li are converged, with respect to the calculated parameters to the precision reported. The binding energy of Li ions is calculated as

$$E_B = \frac{E[Li_xKNb_5O_{13}] - E[KNb_5O_{13}] - xE[Li]}{x} \quad (1)$$

where x is the lithium concentration, $E[Li_xKNb_5O_{13}]$ the energy of lithiated material with a lithium concentration of x (where $x = 0$ corresponds to KNb_5O_{13}), and $E[Li]$ the energy of lithium in its metallic state. The self-interaction of electrons within DFT can result in an artificial delocalization of electrons at metal centers in transition-metal oxides. The DFT+U method is often used to study such materials in Li^+-ion batteries to correct band gaps and/or binding energies.[13,14] However, reported computational studies of pentavalent niobate materials have shown that band gaps and vacancy formation energies computed with pure DFT agree well with the experiment.[14,15] Hence, we have used pure DFT for the calculations reported in this paper.

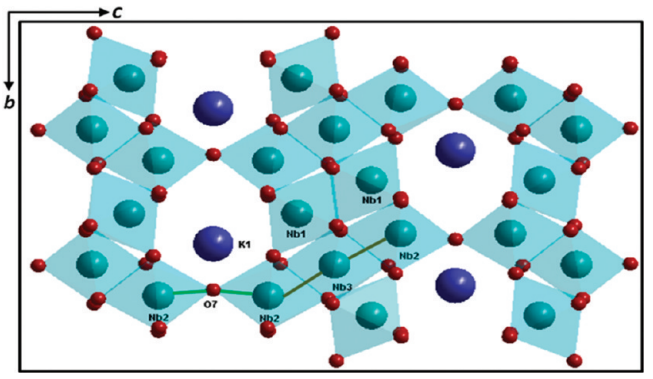

Figure 1. Crystal structure of KNb_5O_{13}.

RESULTS AND DISCUSSION

Lithiation/Delithiation Behavior of KNb_5O_{13}. The charge/discharge curves of a KNb_5O_{13}|Li cell are shown in Figure 3. Upon discharging, the plateau in region B and near-plateau D−E represent two-phase regions separated by a solid-solution range C.

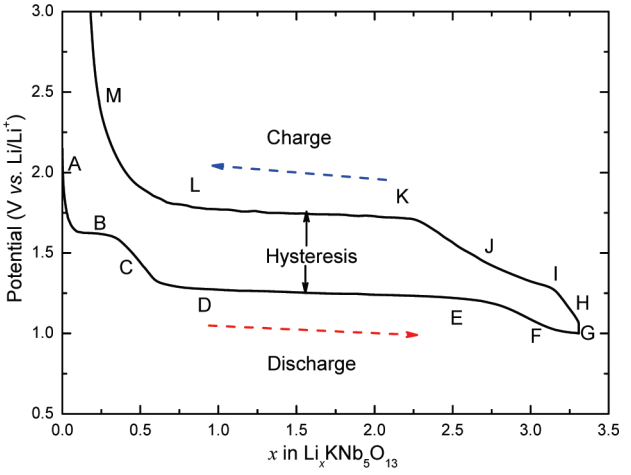

Figure 3. Behavior of lithiation and delithiation in KNb_5O_{13} at a current of 20 mA/g. Points A−M denote the KNb_5O_{13} state corresponding to the XRD and Raman testing.

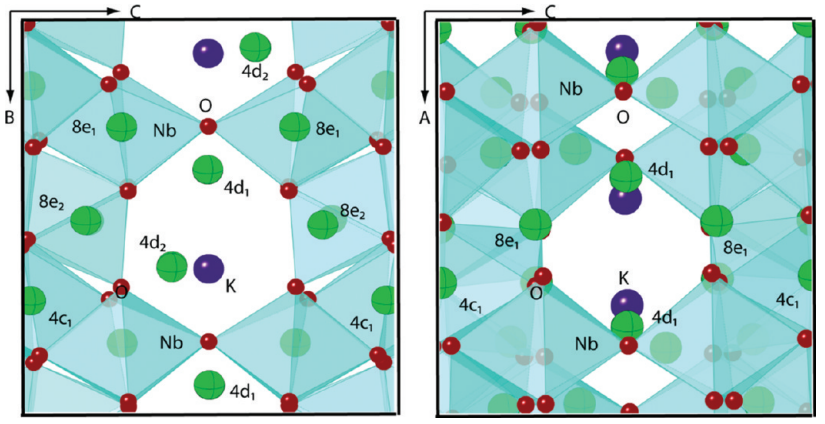

Figure 2. Possible sites for Li intercalation in potassium pentaniobate (KNb_5O_{13}).

dx.doi.org/10.1021/cm200958r |Chem. Mater. 2011, 23, 3210–3216

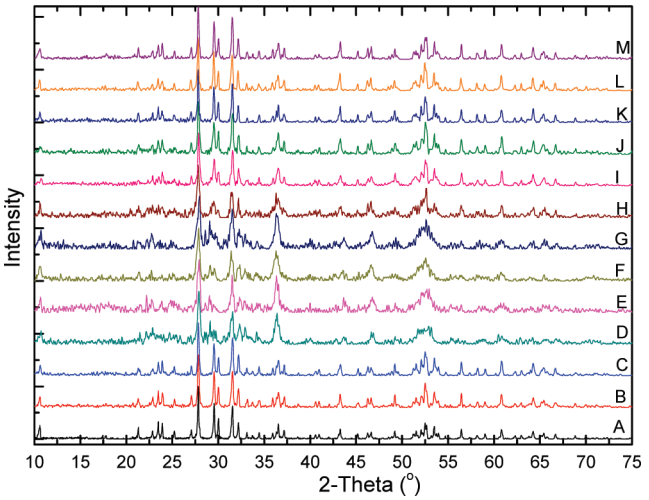

Figure 4. XRD patterns of KNb_5O_{13} in the lithiation/delithiation process.

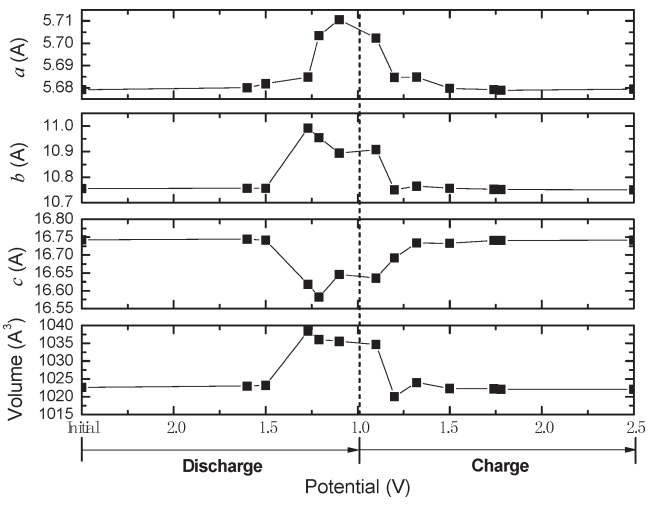

Figure 5. Changes in lattice parameters and volume of KNb_5O_{13} in the process of discharging and charging.

The near-plateau D−E of the discharging appears upon charging in a small range between I and the solid-solution range J, which corresponds to the range C upon discharging, and a large plateau K−L of the charge curve corresponds to the two-phase region B upon discharging. The significant shift in the compositional two-phase regions between discharging and charging gives an unusual, but reproducible hysteresis of the discharge/charge voltage profile. This hysteresis signals a different sequence of occupations of the Li sites in the interstitial space of KNb_5O_{13} upon charging and discharging. Points A−M in Figure 3 are lithiations x at which XRD and Raman testing were performed.

Changes in the Crystal Structure of KNb_5O_{13}. The XRD patterns of Figure 4 show that the insertion of Li^+ ions changes the crystal structure of KNb_5O_{13}. The two (130) and (131) peaks at ~30° split and move to lower angles upon increasing x between points C and D of Figure 3. Four peaks—(220), (221), (213), and (043)—at ~37° overlap each other and form one peak as the lithiation changed to D from C upon discharging, from G to I upon charging. During the delithiation process, all peaks are recovered, which means that all structural changes of KNb_5O_{13} in the charge/discharge process are reversible.

Figure 5 displays the changes in lattice parameters and volume of the $Li_xKNb_5O_{13}$ host as the cell output voltage changes upon charging and discharging. Upon discharging, a large expansion of the b-axis and contraction of the c-axis occurs at 1.5 V > V > 1.25 V within region C; on charge, the b parameter returns to the original length by V = 1.5 V within the solid-solution range J of Figure 3, where the voltage increases across 1.25 V. The total volume change is on the order of 1.5%, because of a 0.1% increase in the a-axis, a 2.2% increase in the b-axis, and a 0.7% decrease in the c-direction. The increase in volume due to lithiation in the range $0.5 \leq x \leq 3.0$ is ~1.25%. Upon charging, the volume decreased across the solid-solution range H, and little volume change occurs from region K to region M. Small lattice-parameter changes indicate Li^+ accommodation in stable sites with little cation−cation repulsion. A sharp increase in the b-axis would appear to signal the onset of Li^+ occupation in a different set of interstitial sites where Li^+−K^+ repulsive forces in the a-axis tunnels displace ions in the b-direction.

Figure 6 shows the two possible tunnels along the a- and b-directions in the KNb_5O_{13} host. Lithiation along the b-axis

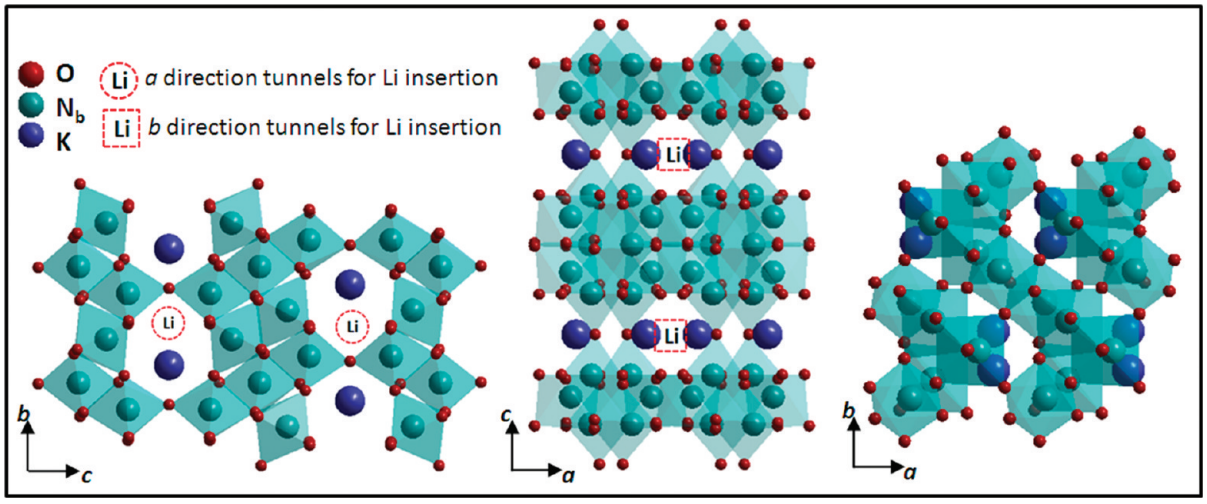

Figure 6. Two possible directions for lithium insertion in KNb_5O_{13}.

dx.doi.org/10.1021/cm200958r |Chem. Mater. 2011, 23, 3210–3216

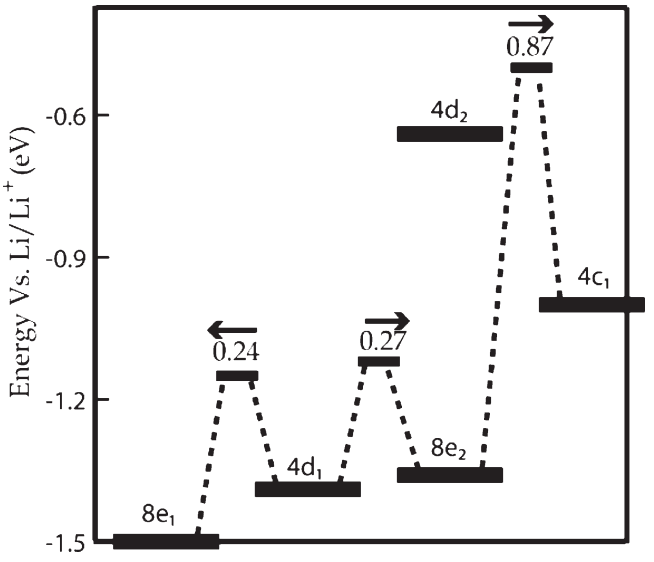

Figure 7. Binding energy and diffusion barriers of Li^+ in KNb_5O_{13} for the sites identified in Figure 2.

tunnels can be expected to produce a large expansion of the lattice parameter *c* because of Li^+-K^+ Coulomb repulsion. The XRD results are against lithiation along the *b*-axis tunnels. Moreover, two K atoms produce a large energy barrier for lithium insertion. Tunnels along the *a*-axis have large open areas for lithium insertion into 4*d* sites, and unoccupied off-axis 8*e* sites within the KNb_5O_{13} slabs can also provide enough space to accommodate inserted lithium. However, only the 4*d* sites of the *a*-axis tunnels can exchange Li^+ with the electrolyte. Nevertheless, why these tunnels with multiple unoccupied sites result in the hysteresis on the charge/discharge curve remains to be considered.

Calculation. *(1). Electronic Structure Calculations.* The lattice parameters of KNb_5O_{13} are calculated as $a = 5.743$ Å, $b = 10.894$ Å, and $c = 16.971$ Å. Compared to the experimental reported lattice parameters ($a = 5.672$ Å, $b = 10.737$ Å, and $c = 16.742$ Å), our DFT calculations slightly overestimate the lattice parameters by 1.5%. $Li_xKNb_5O_{13}$ structures are built by inserting lithium into the calculated host structure and relaxing the volume and ionic positions. In this section, we explore the possible Li binding sites based on the available structural information. Three crystallographically independent Nb ions are present in the crystal; they form three differently distorted octahedral arrangements of oxygens around the niobium. Two out of three different Nb ions occupy 8*e* sites and the third one occupies four 4*c* symmetry sites in the *ab*-plane. One of the independent O^{2-} in the unit cell and the K^+ occupy 4*d* sites in the *ab*-plane. Electronic structure calculations are done to identify the possible sites for Li in the host lattice based on binding energies.

(2). Li-Ion Intercalation. Five different sites are found suitable for Li intercalation in KNb_5O_{13}, two in the *a*-axis channel ($4d_1$ and $4d_2$) and three in the off-axis space between two NbO_6 octahedra ($8e_1$, $8e_2$ and $4c_1$). The identified sites in the host lattice are shown in Figure 2. The binding energies and the energy barriers that separate the identified sites are shown in Figure 7.

The calculated binding energies represent the equilibrium potential for insertion into the identified sites. The calculated values are not in quantitative agreement with measured values; however, taking into account the various intercalation sites and their respective equilibrium potentials, the voltage profile traced from the measured values provide a qualitative description of the measured voltage profile in Figure 3. From the calculated binding energies, the stabilities of the sites for Li intercalation are in the order $8e_1 > 4d_1 > 8e_2 > 4c_1 > 4d_2$. The access of Li^+ into the host structure seems limited to the *a*-axis channel. The most-stable $8e_1$ site can be reached from a $4d_1$ site of the *a*-axis channel. With four formula units per unit cell, there are one $4d_1$ site and two $8e_1$ sites per formula unit. An initial insertion of Li into the $8e_1$ sites via the $4d_1$ sites with diffusion between the $8e_1$ sites via $4d_1$ sites appears to be the lowest-energy diffusion pathway. From the calculated energy barriers that separate the sites (Figure 7), the $8e_1-4d_1-8e_1$ pathway requires less energy than a $4d_1-4d_2-4d_1$ pathway within the *a*-axis tunnel. Although the $8e_2$ sites are also accessible from the $4d_1$ sites, it would appear that one $4d_1$ and two $8e_1$ sites/formula unit are the lowest-energy sites accessible to Li^+ from the electrolyte via the *a*-axis tunnels. However, occupancy of all the $8e_1$ sites is inhibited by Li^+-Li^+ repulsions. Ordering of the Li^+ into every other $8e_1$ site on each side of an *a*-axis tunnel corresponds to one-quarter filling of the $8e_1$ sites; the remaining $8e_1$ sites are destabilized relative to the $4d_1$ sites of the *a*-axis tunnels. Therefore, we interpret plateau B of Figure 3 to represent a two-phase region between Li-poor and Li-rich phases in which the Li-rich phase contains ordered Li^+ in one-quarter of the $8e_1$ sites. It is quite remarkable that occupation of these $8e_1$ sites by Li^+ creates such a small change in lattice volume.

Region C is a single-phase region in which $4d_1$ sites are being occupied. Coulomb repulsive forces push the Li^+ and K^+ apart by displacing them along the *b*-axis, so a remarkable expansion of the *b*-axis, relative to the *a*-axis expansion, is observed in Figure 5 through region C; however, with filling of the $4d_1$ sites, a new Li-rich ordered phase appears in which every other of the remaining empty $8e_1$ sites is occupied, leaving one-quarter of the $8e_1$ sites empty, corresponding to 0.5 Li^+ per formula unit. The pseudo two-phase region D−E of Figure 3 appears to have this Li^+-rich phase as its limiting composition to give 1.5 $8e_1$ and 1 $4d_1$ Li^+ per formula unit, which would correspond to $x = 2.5$. The observed limiting *x* is slightly larger and the D−E region is not completely flat, marking it a pseudo two-phase region. This observation suggests that some $8e_2$ sites are being occupied to increase the limiting *x*; $8e_2$ sites are becoming occupied before all the sample has $x = 2.5$. For $x > 2.5$, $8e_2$ sites become occupied to increase sharply the *a* axis due to interaction between Li^+ ions in occupied $8e_2$ and $8e_1$ sites, interactions that order the Li^+ ions in $8e_2$ sites at G of Figure 3.

(3). Proposed Intercalation/Deintercalation Model. From Figure 7 and the KNb_5O_{13} structure in Figures 1 and 2, the lowest-energy $8e_1$ sites are accessed from the electrolyte and to each other via the $4d_1$ sites. Therefore, the plateau B of the discharge curve of Figure 3 should correspond to a two-phase region involving only $8e_1$ sites: one a Li^+-rich and the other a Li^+-poor phase. The Li^+-rich phase would penetrate from the particle surface; the Li^+-poor phase would be in the interior of the cathodes. Ordering of the Li^+ in the $8e_1$ sites raises the energy of the empty $8e_1$ sites above that of the $4d_1$ sites, so occupancy of the $4d_1$ sites occurs in the solid-solution range C of Figure 3 until a new ordering of Li^+ in the $8e_1$ sites is stabilized. Ideally, the end member of this Li^+-rich phase would correspond to a composition E with $x = 2.5$, where all $4d_1$ and three-quarters of the $8e_1$ sites are occupied by Li^+. The drop in voltage from region E to region G would then be due to filling of $8e_2$ sites. Since the $8e_2$ sites also access the $4d_1$ sites, the removal of the Li^+ ion from $8e_2$ sites via the $4d_1$ sites is followed by the removal of Li^+ from $4d_1$ sites, which leaves the $8e_1$ sites filled at an

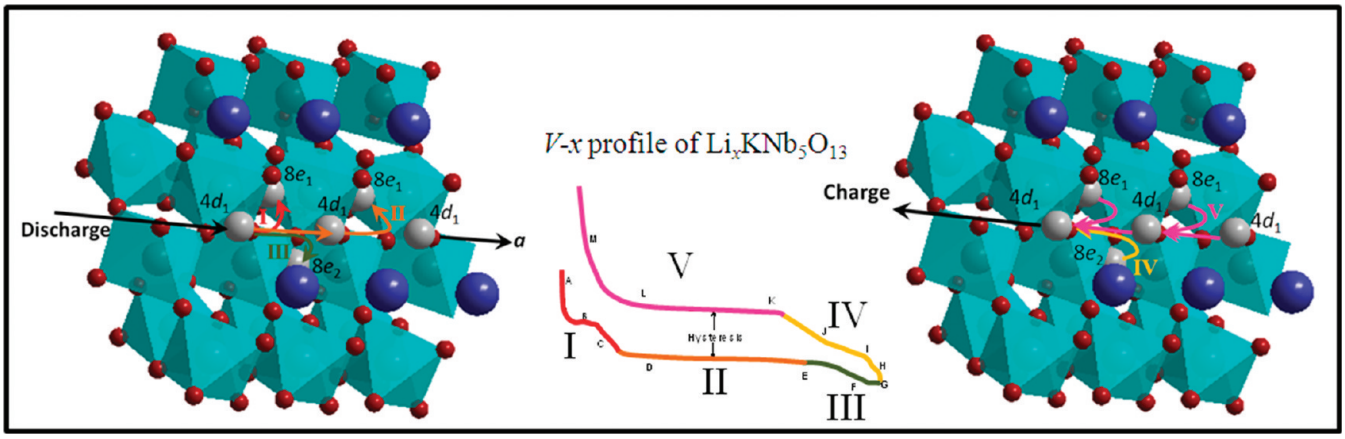

Figure 8. Proposed lithiation/delithiation model of KNb_5O_{13}.

Table 1. Application of the Factor Group Analysis to the External Modes

atom and site symmetry		t'	f'	representation corresponding to the site symmetry	representation corresponding to the factor group D_{2h}
K (4*d*)	C_s	2	8	A' (T_x,T_y)	$2A_g + 2B_{1g} + 2B_{2u} + 2B_{3u}$
		1	4	A''(T_z)	$B_{2g} + B_{3g} + A_u + B_{1u}$
Nb_1, Nb_2 (8*e*)	C_1	3	24	A(T_x,T_y,T_z)	$3A_g + 3B_{1g} + 3B_{2g} + 3B_{3g}$ $+ 3A_u + 3B_{1u} + 3B_{2u} + 3B_{3u}$
Nb_3(4*c*)	C_2	1	4	A(T_z)	$A_{1g} + B_{3g} + A_u + B_{3u}$
		2	8	B(T_x,T_y)	$2B_{1g} + 2B_{2g} + 2B_{1u} + 2B_{2u}$

$x \approx 2$ corresponding to composition K of Figure 3. Removal of the Li^+ from the $4d_1$ sites lowers the *b*-axis. Plateau L−K corresponds to plateau B of the discharge curve, but with ordering of the Li^+ ion in the Li-poor phase, down to $x \approx 0.5$. This model accounts for the anomalous hysteresis of the discharge/charge voltage profile of Figure 3 since the occupancy of the $4d_1$ sites having direct access to the electrolyte is present at different lithium concentrations in the discharge and charge processes. However, the lattice-parameter changes of Figure 5 indicate that the apparent D−E plateau is not flat and that some occupancy of $8e_2$ sites occurs increasingly with *x* in this compositional range on discharging. The proposed lithiation/delithiation process is shown in Figure 8.

Raman Spectra. The lithiation and delithiation process of the Li guest in the KNb_5O_{13} host is evaluated by Raman spectroscopy, which gives the normal modes of vibration and structural information of the host at the atomic scale. The space group and point-group symmetry of KNb_5O_{13} are orthorhombic *Pbmc* (No. 57) and D_{2h}; there are four molecules in a crystallographic unit cell with 76 atoms.[7] Table 1 lists the essential symmetry elements of K and Nb atoms that occupy 4*d*, 4*c*, and 8*e*, respectively. These elements contribute to the external (lattice) vibration modes. Nb atoms are distributed over three sites with two sets of symmetry (C_1, C_2). Nb_2(8*e*) and Nb_3 (4*c*) form edge-shared octahedra site triples with Nb_2−O−Nb_2 bridges between *a*−*b* slabs. The Nb_1(8*e*) bridge the triples via shared corners. The NbO_6 octahedra form the internal vibration modes. From the factor-group correlation analysis,[16] the irreducible representations for KNb_5O_{13} are demonstrated in Tables 1 and 2.

Table 2. Application of the Factor Group Analysis to the Internal Modes

point O_h	site group	factor group D_{2h}
Nb_1, Nb_2	C_1	
$A_{1g}(\nu_1) \rightarrow$	A (× 8)	
$E_g(\nu_2) \rightarrow$	$2A$ (× 8)	
$F_{1u}(\nu_3) \rightarrow$	$3A$ (× 8)	
$F_{1u}(\nu_4) \rightarrow$	$3A$ (× 8)	$(A_g + B_{1g} + B_{2g} + B_{3g}$ $+ A_u + B_{1u} + B_{2u} + B_{3u})$(× 15)
$F_{2g}(\nu_5) \rightarrow$	$3A$ (× 8)	
$F_{2g}(\nu_6) \rightarrow$	$3A$ (× 8)	
Nb_3	C_2	
$A_{1g}(\nu_1) \rightarrow$	A (× 4)	$(A_g + B_{3g} + A_u + B_{3u})$(× 3)
$E_g(\nu_2) \rightarrow$	$2A$ (× 4)	
$F_{1u}(\nu_3) \rightarrow$	$A + 2B$ (× 4)	
$F_{1u}(\nu_4) \rightarrow$	$A + 2B$ (× 4)	$[(A_g + B_{3g} + A_u + B_{3u}) + 2 \times$ $(B_{1g} + B_{2g} + B_{1u} + B_{2u})]$ (× 4)
$F_{2g}(\nu_5) \rightarrow$	$A + 2B$ (× 4)	
$F_{2g}(\nu_6) \rightarrow$	$A + 2B$ (× 4)	

In summary, the irreducible representation of KNb_5O_{13} corresponding to its Raman active vibration can be expressed as $\Gamma_{Raman}(KNb_5O_{13}) = 28A_g + 30B_{1g} + 29B_{2g} + 27B_{3g}$ after taking the acoustical modes into account.

dx.doi.org/10.1021/cm200958r |*Chem. Mater.* 2011, 23, 3210–3216

Therefore, as many as 114 bands are expected in the Raman spectrum of KNb_5O_{13}. However, the number of peaks in the experimental spectrum is less than 114 because several bands overlap each other to form some broad peaks. As for the characteristic peaks of the internal vibration modes of NbO_6,[17,18] the major Raman bands appear in the 600−650 cm^{-1} region and a shoulder appearing in the 520−580 cm^{-1} region is assigned to the symmetric stretching mode of the NbO_6 octahedra. Raman bands at 850−920 cm^{-1} are assigned to the antisymmetric stretching modes of the $Nb_2-O_7-Nb_2$ linkage. In addition, the bending modes of the $Nb_2-O_7-Nb_2$ linkage appear at 408 and 454 cm^{-1}. Peaks lower than 400 cm^{-1} correspond to the external vibration modes of KNb_5O_{13}.

Table 3. Type and Raman Activities of the Normal Modes of KNb_5O_{13}

type	Raman active	Raman inactive
Internal modes of NbO_6	22 A_g	22 A_u
	23 B_{1g}	23 B_{1u}
	23 B_{2g}	23 B_{2u}
	22 B_{3g}	22 B_{3u}
	12 stretching and 78 bending	
External modes of KNb_5O_{13}	6 A_g	4 A_u
	7 B_{1g}	6 B_{1u}
	6 B_{2g}	5 B_{2u}
	5 B_{3g}	6 B_{3u}
Acoustical modes	$B_{1u} + B_{2u} + B_{3u}$	

$$\Gamma_{Raman}(KNb_5O_{13}) = 28A_g + 30B_{1g} + 29B_{2g} + 27B_{3g}$$

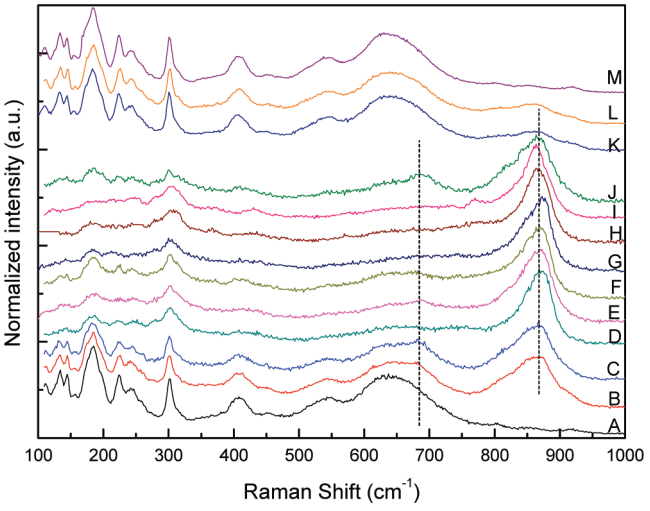

Figure 9. Raman spectra for KNb_5O_{13}.

Figure 9 displays the Raman spectra of KNb_5O_{13} in the lithiation/delithiation process. In the first lithium insertion step from region A (KNb_5O_{13}) to region C ($Li_{0.5}KNb_5O_{13}$), two differences can be observed: (1) a new peak at 684 cm^{-1} appears, and (2) the relative intensity of the antisymmetric stretching of the Nb−O−Nb bridge at 867 cm^{-1} significantly increases. The appearance of the new peak can be attributed to a small distortion of the NbO_6 octahedra. The slight distortion causes only small changes in the lattice parameters of KNb_5O_{13}, as shown in Figure 5. At $x = 0.5$, upon discharging, $4d_1$ sites are occupied in the Li-rich phase near the surface, which pushes the bridging oxygen O_7 from its original position, reducing the $Nb_2-O_7-Nb_2$ angle from 180°. The change in angle changes the intensity of the peak at 867 cm^{-1}.[17] Once Li^+ enter the $8e_2$ sites, the NbO_6 octahedra are distorted drastically. Therefore, a significant change in the lattice parameters of KNb_5O_{13} is observed in Figure 5.[19] The characteristic peaks corresponding to the internal vibration modes of NbO_6 octahedra disappear,[17] but the external lattice modes of the KNb_5O_{13} host remain.

According to our model, upon charging from region G to region J of Figure 3, Li^+ are being removed from $4d_1$ and $8e_2$ sites to make the Raman spectrum at region J similar to that at region C upon discharging. Upon further removal of Li, the plateau K−L of charging should correspond to plateau B of discharge, where only $8e_1$ sites are occupied and the NbO_6 octahedra are less distorted, so the peaks at 546.8 cm^{-1} and 639.8 cm^{-1} reappear.

XPS Analysis. XPS analyzes the oxidation state of elements on the surface of the $Li_xKNb_5O_{13}$ electrode. Figure 10a shows the XPS spectra of five single phases. Except for the change in the intensities of the spectra, only the peak of Nb($3d_{3/2}$) moves slightly to higher energy during the lithiation process. The oxidation state of Nb is reversible in the discharge/charge process. On the surface of the $Li_xKNb_5O_{13}$ electrode, the valence of Nb maintains a formal value

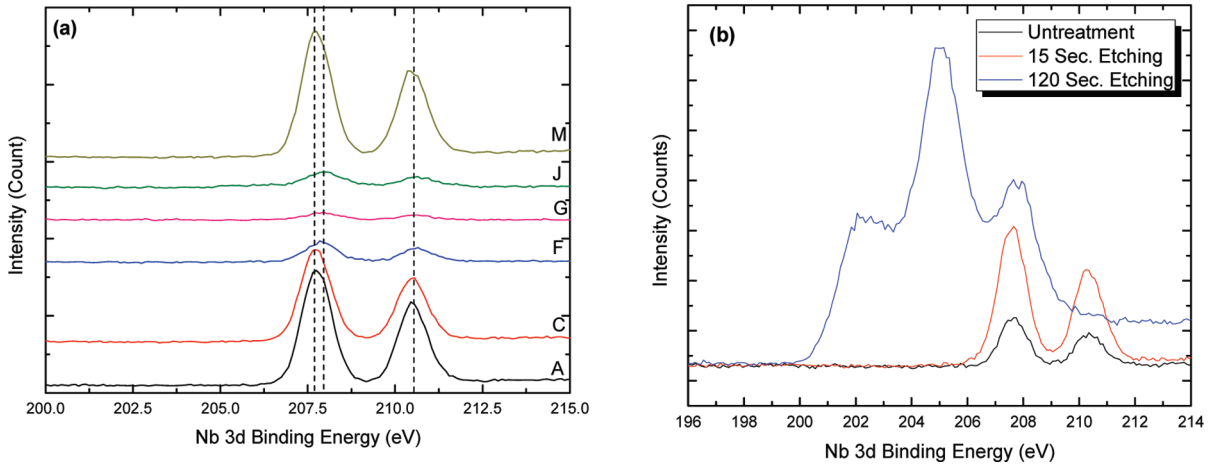

Figure 10. XPS spectra of Nb(3d). A, C, F, G, J, and M correspond to the charge/discharge states listed in Figure 3.

dx.doi.org/10.1021/cm200958r |*Chem. Mater.* 2011, 23, 3210–3216

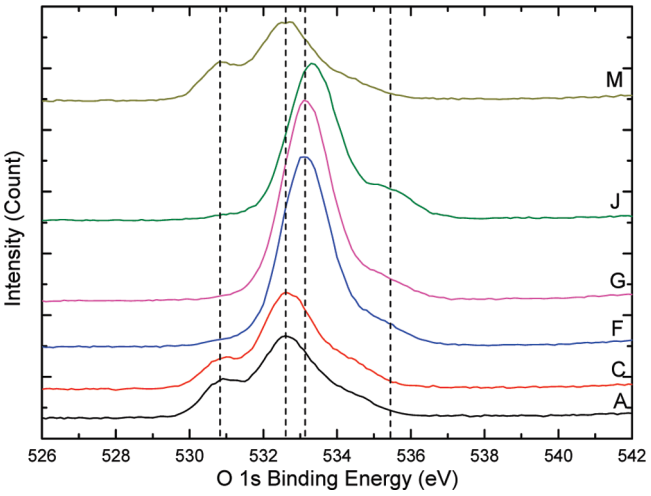

Figure 11. XPS spectra of O(1s). A, C, F, G, J, and M correspond to the charge/discharge states listed in Figure 3.

of +5, the electrons would be stabilized in Nb−Nb bonds across shared octahedral-site edges within the bulk. Argon plasma was employed to remove the surface of the electrode. After a 15-s etch, the oxidation state of Nb in sample F retains the higher valence, but Nb^{4+} was observed in the electrode experiencing a 120-s argon-plasma etch (see Figure 10b).

The oxygen atoms are located in two different environments: corner-sharing and edge-sharing octahedra. Therefore, there are two O(1s) peaks shown in Figure11. Insertion of Li^+ pushes these two peaks to higher energy, and the two peaks even overlap in the heavily lithiated samples where the NbO_6 octahedra are drastically distorted and their characteristic vibration peaks disappear from the Raman spectra, as shown in Figure 9.

CONCLUSIONS

The unusual structure of the host KNb_5O_{13} of the $Li_xKNb_5O_{13}$ ($0 \le x \le 3.5$) Li-insertion electrode is responsible for a polarization hysteresis in the discharge/charge voltage profile after a full discharge to over 3 Li/formula unit. The host KNb_5O_{13} contains one-dimensional *a*-axis tunnels for Li^+ access to the host from the electrolyte, but off-axis interstitial $8e_1$ and $8e_2$ sites have energies for Li^+ occupancy that are comparable to that of the $4d_1$ *a*-axis sites. Computation shows that the stability of the Li^+ is the greatest in the $8e_1$ sites, with their stability in $4d_1$ sites being greater than that in the $8e_2$ sites. Both the $8e_1$ and $8e_2$ sites have access to the electrolyte through the $4d_1$ sites. Upon discharge, ordering of the Li^+ in one-quarter of the $8e_1$ sites destabilizes the empty $8e_1$ sites relative to the $4d_1$ sites is a Li-rich phase; before $x = 0.5$, $4d_1$ sites become occupied in the Li-rich phase until a new Li^+-rich phase is formed with all $4d_1$ sites occupied and an ordered one-quarter of the $8e_1$ sites empty. The remaining empty $8e_1$ sites are destabilized, relative to the $8e_2$ sites, which become occupied where $x > 2.5$ is found. Since only the Li^+ ions in the *a*-axis tunnels of the structure have access to the electrolyte, a subsequent charge first removes the $8e_2$ Li^+, followed by the $4d_1$ Li^+, before the Li^+ in $8e_1$ sites are removed. The difference in the sequence of site occupations upon charging and discharging gives an unusual hysteresis to the discharge/charge $V-x$ profile. The theoretical assignments of site occupancies are shown to be consistent with structural changes and the electrochemical profile. Ordering of the Li^+ in the $8e_1$ sites is responsible for a change in the relative stabilities of the $4d_1$ and $8e_1$ sites upon discharging and charging.

AUTHOR INFORMATION

Corresponding Author

*E-mail address: jgoodenough@mail.utexas.edu.

ACKNOWLEDGMENT

This work was supported as part of the program "Understanding Charge Separation and Transfer at Interfaces in Energy Materials (EFRC: CST)", an Energy Frontier Research Center funded by the U.S. Department of Energy Office of Science, Office of Basic Energy Sciences, under Award No. DE-SC0001091.

REFERENCES

(1) Mizushima, K; Jones, P. C.; Wiseman, P. J.; Goodenough, J. B. *Mater. Res. Bull.* **1980**, *15*, 783.
(2) Thackeray, M. M.; David, W. I. F.; Bruce, P. G.; Goodenough, J. B. *Mater. Res. Bull.* **1983**, *18*, 461.
(3) Manthiram, A.; Lee, S. -J.; Goodenough, J. B. *J. Solid State Chem.* **1987**, *71*, 349.
(4) Padhi, A. K.; Najundaswamy, K. S.; Goodenough, J. B. *J. Electrochem. Soc.* **1997**, *144*, 1188.
(5) Han, J.-T.; Liu, D.-Q.; Song, S.-H.; Kim, Y.; Goodenough, J. B. *Chem. Mater.* **2009**, *21*, 4753.
(6) Srinivasan, V.; Newman, J. *Electrochem. Solid-State Lett.* **2006**, *9*, A110.
(7) Kwak, J.; Yun, H.; Chae, H. K. *Acta Crystallogr., Sect. E: Struct. Rep. Online* **2005**, *E61*, i132.
(8) Lutterotti, L.; Matthies, S.; Wenk, H. R.; Schultz, A. J.; Richardson, J. *J. Appl. Phys.* **1997**, *81*, 594.
(9) Kresse, G; Furthmller, J *Comput. Mater. Sci.* **1996**, *6*, 15.
(10) Kresse, G; Furthmller, J *Phys. Rev. B* **1996**, *54*, 11169.
(11) Perdew, J. P.; Burke, K.; Ernzerhof, M. *Phys. Rev. Lett.* **1996**, *77*, 3865.
(12) Blchl, P. E. *Phys. Rev. B* **1994**, *50*, 17953.
(13) Zhou, F.; Cococcioni, M.; Marianetti, C. A.; Morgan, D.; Ceder, G. *Phys. Rev. B* **2004**, *70*, 235121.
(14) Xu, H.; Lee, D.; He, J.; Sinnott, S.; Gopalan, V.; Dierolf, V.; Phillpot, S. *Phys. Rev. B* **2008**, *78*, 174103.
(15) Veithen, M.; Ghosez, P. *Phys. Rev. B* **2002**, *65*, 214302.
(16) Nakamoto, K. *Infrared and Raman Spectra of Inorganic and Coordination Compounds, Part A: Theory and Application in Inorganic Chemistry*, 6th ed.; John Wiley & Sons: Hoboken, NJ, 2009; pp125−133.
(17) Jehng, J.; Wachs, E. *Chem. Mater.* **1991**, *3*, 100.
(18) Bizeto, M. A.; Leroux, F.; Shiguihara, A. L.; Temperini, M. L. A.; Sala, O.; Constantino, V. R. L. *J. Phys. Chem. Solids* **2009**, *71*, 560.
(19) Peled, E.; Golodnitsky, D.; Ardel, G.; Eshkenazy, V. *Electrochim. Acta* **1995**, *40*, 2197.